

Numerical simulation of two-dimensional flow over a heated carbon surface with coupled heterogeneous and homogeneous reactions

Ryan Federick Johnson & Harsha Kumar Chelliah

To cite this article: Ryan Federick Johnson & Harsha Kumar Chelliah (2017) Numerical simulation of two-dimensional flow over a heated carbon surface with coupled heterogeneous and homogeneous reactions, Combustion Theory and Modelling, 21:1, 2-22, DOI: [10.1080/13647830.2016.1210236](https://doi.org/10.1080/13647830.2016.1210236)

To link to this article: <https://doi.org/10.1080/13647830.2016.1210236>



Published online: 19 Sep 2016.



Submit your article to this journal [↗](#)



Article views: 230



View related articles [↗](#)



View Crossmark data [↗](#)

Numerical simulation of two-dimensional flow over a heated carbon surface with coupled heterogeneous and homogeneous reactions

Ryan Federick Johnson and Harsha Kumar Chelliah*

Department of Mechanical and Aerospace Engineering, University of Virginia, Charlottesville, USA

(Received 31 January 2016; accepted 2 July 2016)

For a range of flow and chemical timescales, numerical simulations of two-dimensional laminar flow over a reacting carbon surface were performed to understand further the complex coupling between heterogeneous and homogeneous reactions. An open-source computational package (OpenFOAM®) was used with previously developed lumped heterogeneous reaction models for carbon surfaces and a detailed homogeneous reaction model for CO oxidation. The influence of finite-rate chemical kinetics was explored by varying the surface temperatures from 1800 to 2600 K, while flow residence time effects were explored by varying the free-stream velocity up to 50 m/s. The reacting boundary layer structure dependence on the residence time was analysed by extracting the ratio of chemical source and species diffusion terms. The important contributions of radical species reactions on overall carbon removal rate, which is often neglected in multi-dimensional simulations, are highlighted. The results provide a framework for future development and validation of lumped heterogeneous reaction models based on multi-dimensional reacting flow configurations.

Keywords: carbon surface reaction; multi-dimensional simulation; reacting boundary layers

1. Introduction

Coupled heterogeneous and homogeneous reactions of carbon surfaces have been extensively investigated in the context of char oxidation in coal combustors [1,2], soot oxidation in propulsion systems [3–6], and thermal protection layer ablation in reentry vehicles [7,8]. In char oxidation investigations, fluid dynamical effects are often simplified by spherical symmetric approximation [9–12]. For flows dominated by radial diffusion, the interaction between homogeneous and heterogeneous reactions leading to distinct combustion regimes have been identified [1,2]. These studies led to the development of lumped surface reaction models for both non-porous [13–15] and porous char [16,17]. Attempts to relax lumped surface reaction models to include elementary reaction steps involving intermediate surface adsorbed species have met limited success, mainly due to lack of species measurements near the reacting surface [18,19]. Thus, considerable uncertainty exists in reaction pathways that describe CO and CO₂ formation near reacting surfaces [1,2]. Efforts are underway to characterise the species profiles in diffusion–reactive layers above reacting surfaces [20] and this paper describes a parallel modelling effort supporting such experiments.

Several studies have proposed heterogeneous surface reaction models for both non-porous graphite (compiled in [15]) and porous carbon [17]. These heterogeneous models

*Corresponding author. Email: harsha@virginia.edu; Tel: +1 (434) 924-6037, Fax: +1 (434) 982-2037

consist of semi-global reactions that depend on the surface physical properties and local temperature and species concentrations. For high surface temperatures (greater than 1500 K), the main product is carbon monoxide, CO, which reacts with gaseous oxygen, O₂, to form carbon dioxide, CO₂. The CO₂ formed in the gas-phase diffuses to the surface and reacts with the carbon surface to create additional CO [1,2]. Extensive modelling work has been performed by various groups by implementing detailed kinetic models in an effort to understand these homogeneous–heterogeneous coupling mechanisms better [17,18,21–23]. Although the canonical reacting flow configurations selected were simple and computationally efficient, they can only be used to predict reactions and transport effects in one- or quasi-one-dimensional analysis. More recently, multidimensional reacting carbon surfaces were considered in graphite nozzle ablation studies [24–27]. Although the results of these studies showed the multidimensionality of reacting carbon surfaces, several assumptions were made, namely the removal of O₂ and O reactions with carbon, that make their results inapplicable to carbon surfaces reacting in air.

To our knowledge, only limited detailed investigations have been performed on the multidimensional effects of reacting carbon surfaces in an oxidising environment [28]. Specifically, the lack of fundamental investigations of the multidimensionality effects of coupled heterogeneous and homogeneous reactions on carbon surfaces is the main motivation of the present work. Here, we consider a two-dimensional laminar reacting boundary layer over a heated carbon surface, which is one of the most common geometries used in investigating homogeneous reacting boundary layers with heat and mass transfer. Semi-global carbon surface reaction models were implemented in a reacting flow solver (OpenFOAM®) with detailed homogeneous chemistry and molecular transport [29]. For the assessment of the effects of the coupled gas and surface kinetic rates with fluid dynamics, the surface temperature and free-stream velocity ranged from 1800 to 2600 K and from 30 to 50 m/s, respectively, were investigated. The simulated domain was 10 mm in length and 1 mm in height with a 5 mm long reacting carbon surface.

2. Numerical approach

The OpenFOAM® computational package was used to integrate the following reacting Navier–Stokes equations:

$$\frac{\partial \rho}{\partial t} + \nabla \cdot \rho \vec{v} = 0, \quad (1)$$

$$\frac{\partial \rho \vec{v}}{\partial t} + \nabla \cdot (\rho \vec{v} \vec{v}) = -\nabla p + \nabla \cdot \mathbb{T}, \quad (2)$$

$$\frac{\partial \rho h_s}{\partial t} + \nabla \cdot \rho \vec{v} h_s - \nabla \cdot \rho \alpha \nabla h_s + \nabla \cdot \sum_{i=1}^N \rho h_i^s \vec{V}_i = - \sum_{i=1}^N h_i^o w_i, \quad (3)$$

$$\frac{\partial \rho Y_i}{\partial t} + \nabla \cdot \rho \vec{v} Y_i - \nabla \cdot \rho D_i \nabla Y_i = w_i, \quad (4)$$

where ρ is the density, \vec{v} is the velocity vector, p is the hydrodynamic pressure, \mathbb{T} is the deviatoric stress tensor, h_s is the sensible enthalpy, α is the thermal diffusivity of the mixture, and Y_i , D_i , w_i , $h_i^o w_i$ are the species mass fraction, mixture averaged diffusion coefficient, mass production rate, and heat release rate, respectively. The conservation equations are solved in a time-split, segregated manner using a second-order accurate

total variation diminishing van Leer scheme. The finite volume equations are integrated in time using the first-order implicit, Eulerian method [30]. Simulations are run for a specific number of time integrations until steady state is reached and confirmed by monitoring solution residuals; in this work, residuals are the L2-norm normalised by the initial error.

The homogeneous chemical source term, w_i , is modelled via a moist-CO oxidation kinetic model extracted from JetSurf2.0 [31]. The transport and thermochemical properties are calculated using the same approach as described by the Sandia ChemkinTM and transport packages, respectively [32,33]. In OpenFOAM®, the transport and thermodynamic properties are updated using external subroutines that were integrated into the solver. To save computational cost, only mixture averaged molecular diffusion is implemented. It should be pointed out that our previous work on quasi-one-dimensional analysis of carbon surface oxidation has shown that treatment of species transport via mixture averaged or iterative solution of Stefan–Maxwell equations (equivalent to a multi-component transport property description) is identical in the present moist CO oxidation case [17,23].

There is no computationally efficient approach that can be used to solve explicitly for the pressure field of low Mach number reacting flows. Hence, a pressure implicit splitting of operators (PISO) method [34] is used to iterate between the solved velocity field and a guessed hydrodynamic pressure distribution until a specified numerical tolerance is met. The hydrostatic pressure was treated as a small perturbation from the thermodynamic pressure, which allowed for the decoupling of acoustics from the system of equations [35]. This pressure solving technique is computationally efficient and has precedence in the combustion community (see [22,36,37]). Thermodynamic pressure was held constant, $p_o = 1$ atm, and was used to provide closure in updating the thermodynamic quantities T and ρ through the equation of state.

2.1. Heterogeneous reaction models

The two sets of heterogeneous semi-global reaction models listed in [Tables A1](#) and [A2](#) (see [Appendix A](#)) were used to describe the carbon surface reactions. The models include reactions of carbon atoms at the surface (identified as C_s) with gaseous species O_2 , CO_2 , H_2O , OH , and O atoms. These species react with active carbon sites at the surface, identified as C_s , and produce CO as well as traces of H_2 and H atoms. For non-porous carbon, a surface reaction model compiled by [15] for pure graphite with a density of 2.24 gm/cm^3 was implemented. For porous carbon, an alternative model developed by [17] was implemented in which several reactions of Bradley’s model are tuned to include 25% bulk porosity effects (with a bulk density of 1.8 gm/cm^3). Specifically, only $C_s + O_2$ and $C_s + CO_2$ reactions were tuned to match with experimental results of a porous carbon surface. [Appendix A](#) contains details on these reaction models and implementations.

[Figure 1](#) shows the calculated ratio of the porous to non-porous carbon monoxide production rates for reactions $C_s + \frac{1}{2}O_2 \rightarrow CO$, $C_s + CO_2 \rightarrow 2CO$, and $C_s + H_2O \rightarrow CO + H_2$ as a function of temperature. These reaction rates were calculated using constant reference quantities for density, $\rho = 1.15 \text{ kg/m}^3$, pressure, $p = 1.0 \text{ atm}$, and mixture composition. According to [Figure 1](#), the porous carbon surface reaction rates for O_2 and CO_2 can be two orders of magnitude greater than those of the non-porous model. In particular, for temperatures greater than 2200 K, the ratio of the O_2 reaction rate increases rapidly with increase in temperature. This is due to the annealing phenomenon of carbon oxidation that is accounted for in the Bradley and Dixon-Lewis [15] model and causes the non-porous O_2

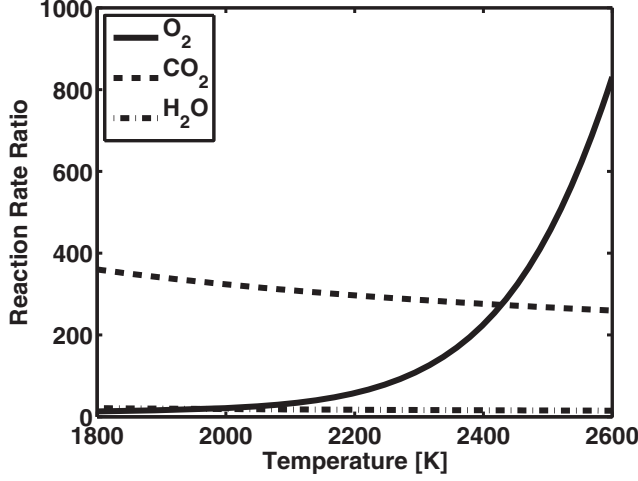


Figure 1. Comparisons of reaction rate ratio of porous reaction rates to non-porous reaction rates for O₂, CO₂, and water for a representative composition and pressure of a gas mixture. Note that H₂O was not tuned in porous model [17].

reaction rates to relax at higher temperatures. Such annealing effects are not included in the porous reaction model as it was validated only up to 2000 K [17].

2.2. Reacting interface boundary condition specification

All surface reactions listed in Tables A1 and A2 were implemented using a derived boundary type based on reactions at an interface [38] which, for this application, is written as

$$\frac{\partial (\rho' Y_i)}{\partial t} + \rho Y_i v_n + \rho D_i \frac{\partial Y_i}{\partial n} - w'_i = 0, \quad (5)$$

where n is the normal direction, v_n is the blowing velocity normal to the surface, ρ' the surface density, and w'_i is the surface reaction source term of species i . In OpenFOAM®, the above species flux equation is solved using an external subroutine. A first-order, up-wind scheme is used for the $\partial Y_i / \partial n$ term. The source term, w'_i is calculated using either the non-porous or porous model as detailed in Appendix A. The subroutine uses the previous values for velocity normal to the reacting surface, v_n , and then it is updated using

$$v_n = \sum_{i=1}^N w'_i / \rho, \quad (6)$$

which assures a unique value for the blowing velocity due to surface reactions; this relationship can also be derived from the continuity equation of a reacting surface. Equation (5) is decoupled from the Navier–Stokes equations in the OpenFOAM® solver. Surface species quantities are solved for by semi-implicitly marching in time according to the surface reaction timescales. These values are then used to update the boundary conditions used by the reacting Navier–Stokes equations.

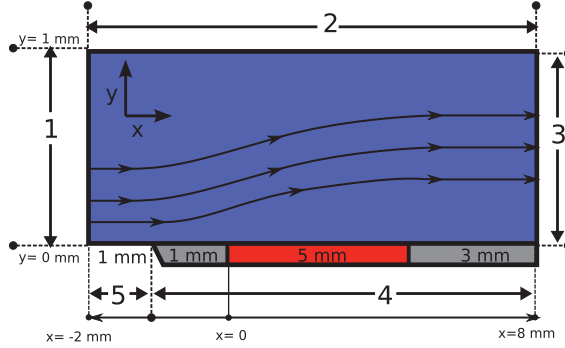


Figure 2. Two-dimensional computational domain used in the present simulations; the 5 mm block at the bottom wall shows where the reacting carbon sample is located. (Colour online)

3. Computational domain and test simulations

An illustration of the two-dimensional computational domain is shown in Figure 2. The lengths of the computational domain are 10 and 1 mm in directions parallel and normal to the surface, respectively. Numerical labels are used to identify each separate boundary condition. The upstream (left) boundary, labelled 1, is where the free-stream values for velocity, oxidiser composition, and temperature are specified as fixed-value conditions. The top and downstream (right) boundaries, labelled 2 and 3, respectively, specify pressure as a far-field boundary condition and all remaining variables are specified as zero-gradients. The lower boundary consists of a 1 mm long open section, which allows for the development of the flow field prior to the leading edge (labelled 5), and a 9 mm long non-slip flat wall (labelled 4) that contains the 5 mm long reacting carbon surface (with a specified surface temperature, T_s). The specific values assigned for all the physical boundary conditions are listed in Table 1. Not listed in this table are the values for free-stream velocity, U_∞ , and surface temperature, T_s , which are the variable input parameters in this investigation. The free-stream composition is specified as $Y_{O_2} = 0.21$, $Y_{H_2O} = 0.02$, and $Y_{N_2} = 0.77$, corresponding to moist air with relative humidity 80%. Excluding the reacting surface where concentrations are calculated as described above, the species boundary conditions are set to zero-gradient.

Table 1. Numerical boundary conditions imposed on five surfaces identified in Figure 2.

Boundary	Pressure [†] (Pa)	Temperature (K)	Velocity (m/s)
1	$\frac{\partial p}{\partial x} = 0$	$T = 320$	$\vec{v} = (U_\infty, 0)$
2	$p_\infty = 0$	$\frac{\partial T}{\partial y} = 0$	$\frac{\partial \vec{v}}{\partial y} = 0$
3	$p_\infty = 0$	$\frac{\partial T}{\partial x} = 0$	$\frac{\partial \vec{v}}{\partial x} = 0$
4	$\frac{\partial p}{\partial y} = 0$	$T = T_s$	$\vec{v} = (0, v_n)$
5	$p_\infty = 0$	$\frac{\partial T}{\partial y} = 0$	$\frac{\partial \vec{v}}{\partial y} = 0$

Note: v_n is calculated from the overall surface reaction rates; $v_n = 0$ where the reactions are turned off.

[†]The pressure here is the reference hydrodynamic pressure.

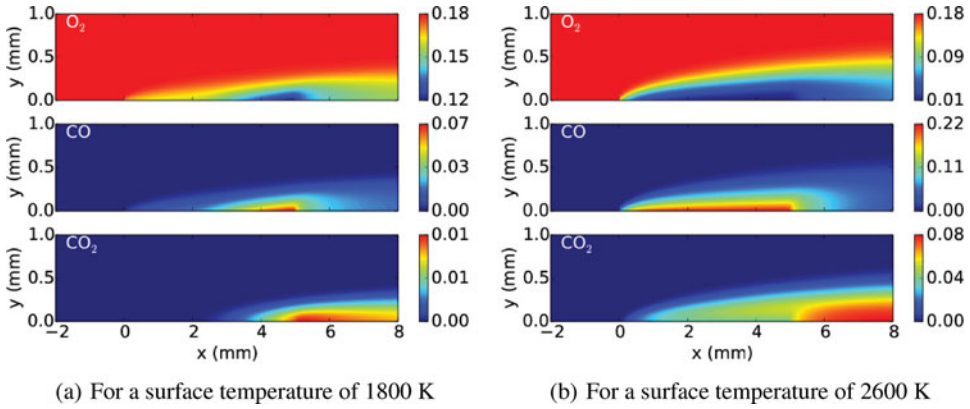


Figure 3. Two-dimensional contour plots of O_2 , CO , and CO_2 for a non-porous carbon surface reaction with a free-stream velocity of 40 m/s.

The finite volume cells employed consist of an aspect ratio of 1 and a size of $10\ \mu\text{m}$, resulting in 100,000 cells for each simulation. Chemical residence time effects were investigated by varying free-stream velocity up to 50 m/s while keeping a fixed surface temperature of 1800 K. This was done for both non-porous and porous surface reaction models. Temperature effects were studied by varying the surface temperature from 1800 to 2600 K for both non-porous and porous models with a free-stream velocity of 40 m/s. Table 2 lists selected simulation results considered in the following discussions.

4. Results and discussion

The converged steady-state solutions of reacting carbon surfaces for a range of free stream velocities and surface temperatures are presented here. For similar surface temperature and flow residence times, the effects of carbon surface porosity is explored by implementing the surface reaction models described in Appendix A. As previously stated, the heterogeneous model for porous carbon provides consumption rates that are orders of magnitudes greater than non-porous graphite. This important difference in model choice determines the contribution each reactant has on the reacting boundary layer profile, as well as the other parametric conditions discussed below.

4.1. Surface temperature effects

For a free-stream velocity of 40 m/s, Figures 3(a) and 3(b) show contour plots of O_2 , CO , and CO_2 mole fractions for the non-porous model at two extreme surface temperatures

Table 2. Parametric values for free-stream velocity and surface temperature explored in the present study.

Surface	Velocity, U_∞ (m/s)	Temperature, T_s (K)
Non-porous	40	[1800, 2000, 2200, 2400, 2600]
Porous	40	[1800, 2000, 2200, 2400, 2600]
Non-porous	[30, 40, 50]	1800
Porous	[30, 40, 50]	1800

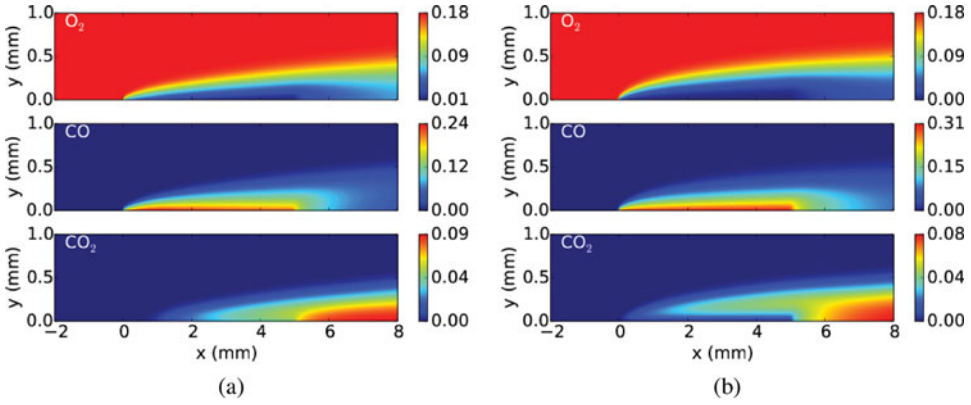


Figure 4. Contour plots of O_2 , CO , and CO_2 for a porous carbon surface reaction with a free-stream velocity of 40 m/s and (a) a surface temperature of 1800 K, (b) a surface temperature of 2600 K.

considered, 1800 and 2600 K, respectively. The higher surface temperature leads to increased carbon consumption at the surface resulting in O_2 depletion near the surface. The CO formed at the surface is oxidised to form CO_2 in the boundary layer, which is highest closest to the surface in the downstream non-reacting surface region (for this high flow velocity). At locations nearest to the surface, the no-slip boundary condition causes the residence time to increase, which allows for the conversion of CO to CO_2 . The increase in temperature also increases the size of the reaction layer due to the increased CO flux from the surface and thermal expansion associated with heat release from CO oxidation in the gas phase.

For the porous carbon surface reaction model corresponding to about 25% porosity [17], a similar set of contour plots is shown in Figures 4(a) and 4(b) for O_2 , CO , and CO_2 mole fractions at two surface temperatures of 1800 and 2600 K. The higher reactivity of O_2 in the porous model causes the O_2 mole fraction to be two orders of magnitude smaller than that of the non-porous case at 1800 K. Similar to that of the non-porous model, for a velocity of 40 m/s, CO_2 is highest in the region downstream of the non-reacting part of the flat surface where the blowing velocity is zero with increased flow residence time.

The coupled effects of porosity and surface temperature controlling the two-dimensional contour plots shown above can be better understood by considering one-dimensional data parallel to the surface. Figures 5(a) and 5(b) show a comparison of the O_2 mole fraction along the surface for non-porous and porous surface reaction models, and for surface temperatures ranging from 1800 to 2600 K with a fixed free-stream velocity of 40 m/s. Additionally, Figures 6(a) and 6(b) show similar results for CO_2 mole fraction variation. At the leading edge of the reacting sample, the porous carbon model shows a depletion of O_2 compared to the non-porous model. Consequently, the mass loss rate towards the leading edge of the porous sample is much higher, leading to a non-uniform regression rate of the surface along the flow path. In both the non-porous and porous cases, the increase in temperature causes a sudden increase in CO_2 with an eventual decrease in concentration at higher temperatures. This is due to the coupling of the surface and gas phase reactions, where at higher temperatures the surface reaction $C_s + CO_2 \rightarrow 2CO$ with a larger activation energy of 64 kcal/mole becomes dominant. For both cases, CO_2 decreased but the porous model has an order of magnitude less CO_2 along the surface due to the stronger reactivity. All of these profiles for species along the reacting surface change with temperature in both

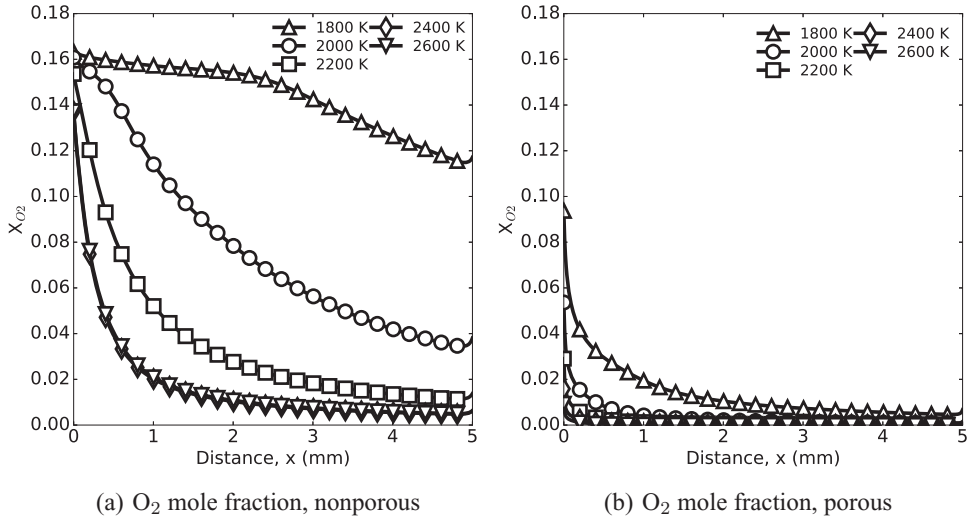


Figure 5. Comparison of O₂ mole fraction along the reacting carbon surface for non-porous and porous models and for temperatures ranging from 1800 to 2600 K.

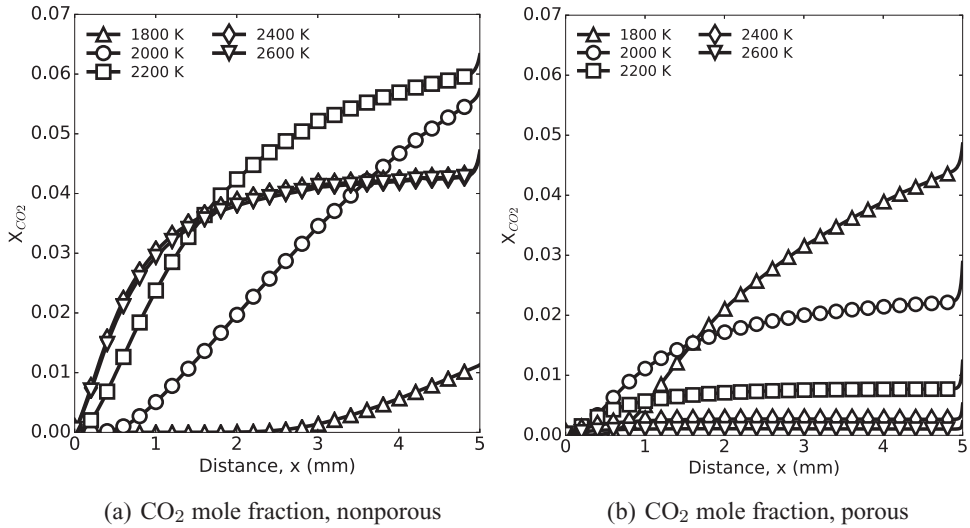


Figure 6. Comparison of CO₂ mole fraction along the reacting carbon surface for non-porous and porous models and for temperatures ranging from 1800 to 2600 K.

magnitude and shape making it necessary to include multidimensionality in carbon surface reactions where transverse flow is present.

4.2. Residence time effects

For a fixed surface temperature of 1800 K and for the non-porous model, Figures 7(a) and 7(b) show contour plots of O₂, CO, and CO₂ mole fractions with free-stream velocities of 30 and 50 m/s, respectively. The influence of lower residence time associated with 50 m/s

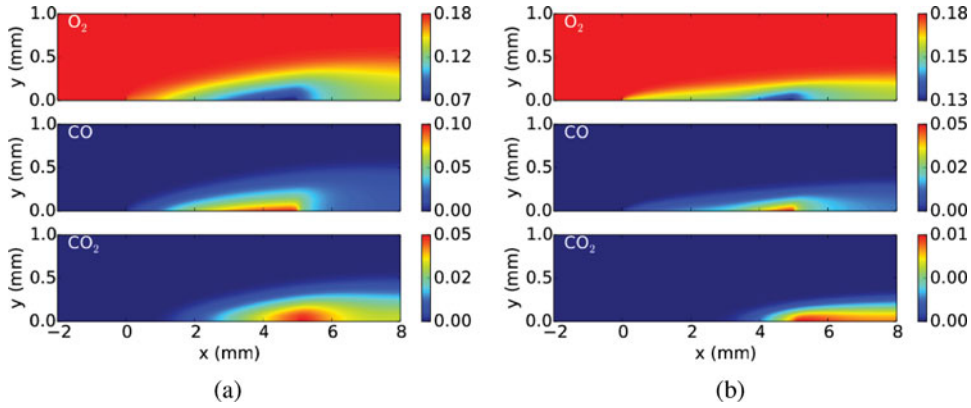


Figure 7. Contour plots of O_2 , CO , and CO_2 for the non-porous surface reaction model, a surface temperature of 1800 K, and free-stream velocities of (a) 30 m/s and (b) 50 m/s.

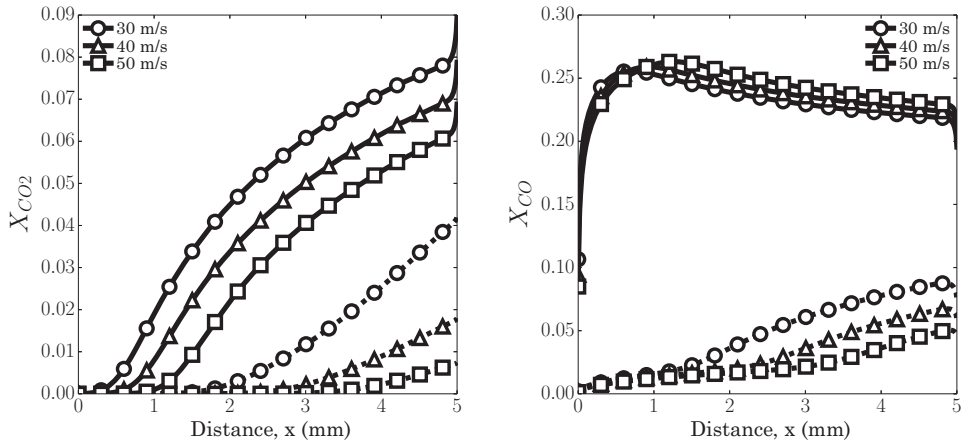


Figure 8. Comparison of CO and CO_2 mole fraction along the reacting carbon surface for non-porous (---) and porous (—) models and for three different free-stream velocities. Surface temperature is at 1800 K.

flow on the gas-phase chemistry is demonstrated by the lack of conversion of CO to CO_2 . This suggests that a balance between diffusive and chemical source terms exists and that a numerical assessment can be utilised to understand local extinction based on overall CO to CO_2 conversion rates. Additionally, an increase in velocity also reduces the CO_2 mixing layer thickness and consequently increases the diffusive velocities normal to the reacting surface.

Once again, line plots of CO and CO_2 along the reacting surface reveal the effects of porosity and varying free-stream velocities on both surface reaction rate producing CO and homogeneous oxidation of CO , as shown in Figures 8(a) and 8(b). For the porous reaction model, velocity variation has a minimal effect on CO mole fraction indicating that the surface reactions are not controlled by transport at 1800 K. In contrast, for the non-porous reaction model, a noticeable influence of flow velocity on CO mole fraction is seen and this can be attributed to the lower reactivity of the O_2 reaction. Oxygen is depleted less in the non-porous reaction and other reactants, OH , O , and CO_2 , become lead contributors in

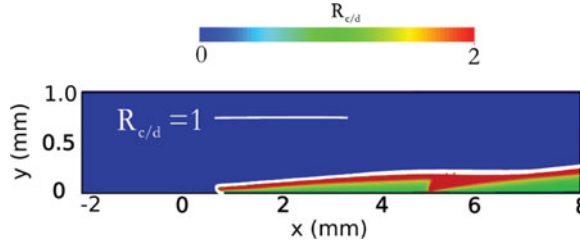


Figure 9. Contour plot of $R_{C/D}$ for CO_2 using the porous surface model, for a free-stream velocity of 50 m/s with a surface temperature of 1800 K.

the production of CO. These other reactants are formed within the reacting layer, which is shifted downstream with increase in free stream velocity. This CO concentration reliance on other reactants is quantified in detail below.

To analyse further the effects of flow residence time versus chemical time, the spatial locations where diffusive and chemical flux terms balance are analysed here. From the steady state species conservation Equation (4), one can extract the following terms, identified here as the ratio of chemical source term to diffusive flux term of species i :

$$R_{C/D,i} = \begin{cases} \frac{w_i}{-\nabla \cdot \rho D_i \nabla Y_i} & \text{for } Y_i > Y_{\min}, \\ 0 & \text{for } Y_i < Y_{\min}. \end{cases} \quad (7)$$

Here, $R_{C/D,i}$ can be treated as an appropriate Damköhler number. In the regions where the species of interest i was less than $Y_{\min} = 10^{-6}$, the term $R_{C/D,i}$ was not evaluated as the chemical reaction rate, w_i , was negligible. In the limit as $R_{C/D,i}$ approaches unity, the chemical source term balances with the diffusive flux term. At this point the convective term, from species conservation, must be negligible. The contour line shown in Figure 9 identifies where $R_{C/D,\text{CO}_2} = 1$. (Note that for the purpose of illustrating $R_{C/D,i} = 1$, the contour plot shown in Figure 9 was limited to a maximum value of 2.0 because higher values were unimportant except that they were large.) The regions where $R_{C/D,i} \leq 1$ can be identified as regions where gas-phase reactions cease to exist or where diffusion terms dominate.

Figures 10(a) and 10(b) show a comparison of the $R_{C/D,\text{CO}_2} = 1$ contour lines for non-porous and porous models. As the free-stream velocity is varied from 30 to 50 m/s, the $R_{C/D,\text{CO}_2} = 1$ contour lines shift in the downstream direction. The distance of this shift is dependent on the surface reaction model implemented. Specifically, for the non-porous reaction model, a shift in $R_{C/D,\text{CO}_2} = 1$ lines is observed with increasing velocity, which is indicative of local extinction occurring. A shift is still apparent for the porous surface reaction model where higher CO fluxes from the surface occur and consequently higher CO_2 production rates are yielded; however, the shift is less than that for the non-porous model. The present velocity range considered does not exhibit a local extinction phenomenon. However, further increase in free-stream velocity is expected to show a behaviour similar to that shown in Figure 10(a).

Although the ratio $R_{C/D,i}$ gives details of the overall response of a reacting surface to free-stream velocity, it does not give detailed information on convective, diffusive, and chemical source term variations. Figures 11(a) and 11(b) show the values of the convective ($\rho v_j \partial Y_{\text{CO}_2} / \partial x_j$), diffusive ($\partial(\rho Y_{\text{CO}_2} V_{\text{CO}_2,j}) / \partial x_j$), and mass production (w_{CO_2}) terms of the species conservation equation of CO_2 as a function of distance normal to the reacting

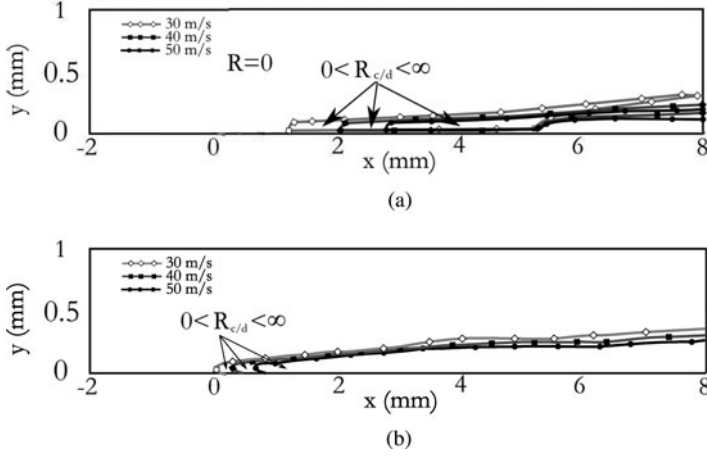


Figure 10. Contour plots of $R_{C/D}$ for CO_2 for three different free-stream velocities of 30, 40, and 50 m/s with a surface temperature 1800 K: (a) non-porous surface model; (b) porous surface model.

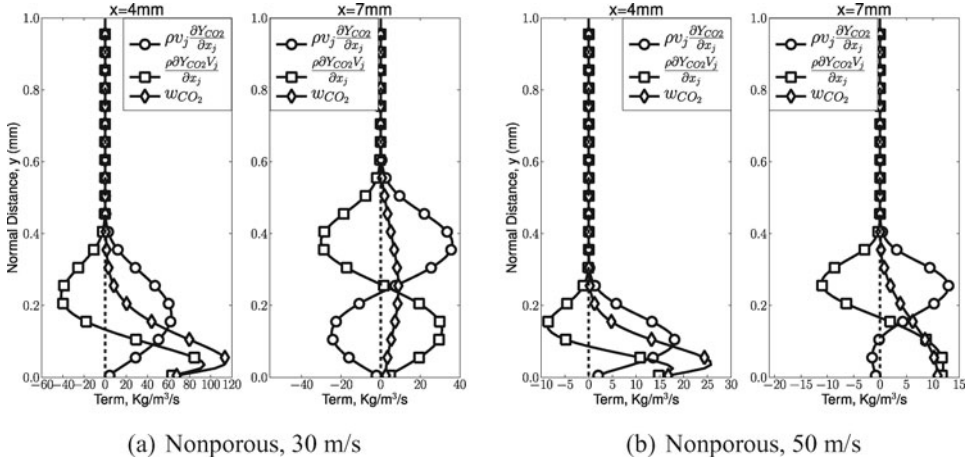


Figure 11. Terms of the species conservation equation for CO_2 (Equation 4) for the non-porous model with 30 and 50 m/s free-stream velocities and a surface temperature of $T_s = 1800$ K.

surface, for the non-porous cases at 30 and 50 m/s, respectively. The data presented here were sampled at two stream-wise locations along the reacting surface, namely at $x = 4$ and 7 mm.

Close to the reacting surface, the convective terms are negligible, hence the diffusive and mass production terms balance each other. As the distance from the surface increases, the reactivity diminishes and the convective and diffusive terms dominate. This is due to the decrease in temperature and increase in velocity within the momentum and thermal boundary layers. The non-reacting region has very small mass production rates, as CO is not produced at that location. The heights of these active layers decrease with increase in velocity. For example, the non-porous case reduces from a height of 0.6 to 0.4 mm, whereas the porous case reduces from 0.7 to 0.55 mm at $x = 7$ mm. This is due to the thinning of the thermal boundary layer, which decreases reactivity at distances normal to the surface.

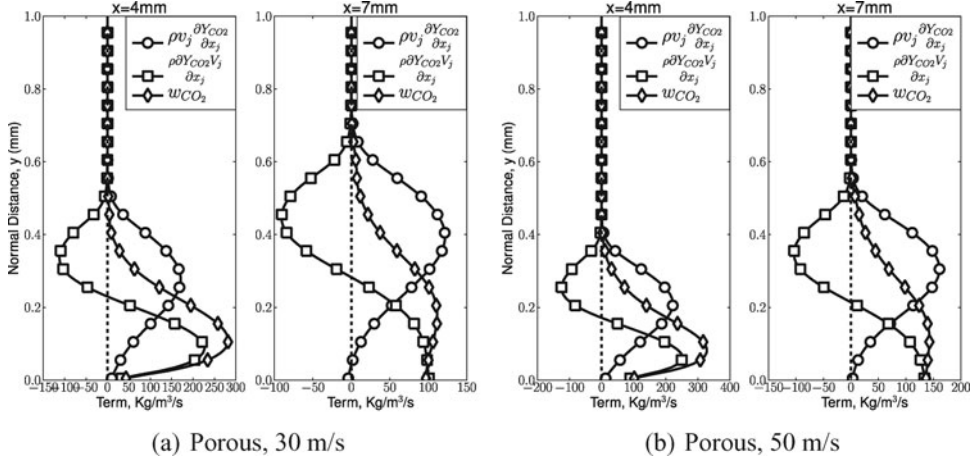


Figure 12. Terms of the CO_2 conservation equation (Equation 4) for the porous model with 30 and 50 m/s inflow velocities and a surface temperature $T_s = 1800$ K.

In addition, the decreased momentum boundary layer with increasing free-stream velocity causes the convective terms to dominate closer to the surface. This changes the overall balance in CO_2 's conservation equation and subsequently reduces CO_2 's peak values.

4.3. Coupling between heterogeneous and homogeneous reactions

As described in Appendix A, typically five semi-global heterogeneous reactions are used to describe the reactions occurring at the carbon surfaces. These five reactions correspond to active carbon sites reacting with O_2 , CO_2 , O , OH , and H_2O ($k = 1, \dots, 5$). The relative importance of these reactions depends on the application. For example, in soot oxidation under fuel-rich conditions, the $\text{C}_s + \text{OH}$ reaction is found to be more important compared to the $\text{C}_s + \text{O}$ reaction because of the availability of OH over O atoms [39,40]. In the present application, the relative contributions between the gas-phase species interacting with active carbon sites are quantified, for a range of parametric conditions.

The overall CO production rate at the surface, w'_{CO} , can be written in terms of the contributing semi-global reactions as

$$w'_{\text{CO}} = \sum_{k=1}^5 \nu_k \frac{W_{\text{CO}}}{W_k} s'_k, \quad (8)$$

where W_{CO} is the molecular weight of CO , W_k is the molecular weight of the homogeneous reacting species, ν_k is the stoichiometric coefficient of CO in the heterogeneous reaction corresponding to species k , and s'_k is the surface mass production rate of species k . Based on the above definition for overall CO production, one can calculate the fraction of CO production due to the five contributing homogeneous species as

$$\Phi_k = \nu_k \frac{W_{\text{CO}}}{W_k} s'_k / w'_{\text{CO}}. \quad (9)$$

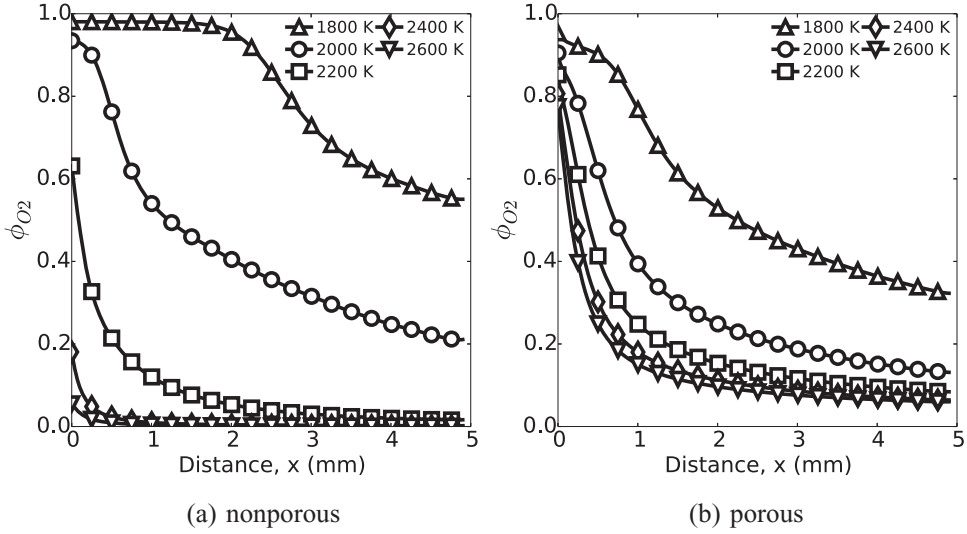


Figure 13. Fraction of CO production due to reaction with O_2 , for a velocity of 40 m/s and range of surface temperatures.

Figures 13(a) and 13(b) show the fraction that O_2 contributes to overall CO production along the surface, for temperatures ranging from 1800 to 2600 K, a free-stream velocity of 40 m/s, and for non-porous and porous surface reaction models, respectively. It is clear that O_2 contributes more than 80% of CO production at the leading edge of the reacting surface for both models and at lower temperatures. As the temperature increases, Φ_{O_2} decreases due to the increased contributions by other reactions and the establishment of a gas-phase CO– O_2 flame leading to production of CO_2 . O_2 is consumed along the surface and is not reproduced by gaseous reactions, which lowers its contribution to CO production in the transverse direction.

The most interesting finding is that, for the non-porous reaction model with a much lower CO production rate, the fractional contribution due to the $C_s + OH$ and $C_s + O$ reactions dominate over the $C_s + CO_2$ reaction. Comparatively, the fraction of CO production of O_2 for high temperatures in the non-porous model is less than that of the porous model. This not due to depletion of O_2 through consumption over the reacting surface, but due to the increase in contributions of OH and O-atom concentrations for CO production. Figures 14(a) and 14(b) show the production of CO due to OH and Figures 15(a) and 15(b) show the production of CO due to O atoms. Depending on temperature, OH and O atoms collectively produce 20 to 40% more of the CO than in the porous case. As previously mentioned, $C_s + O_2$ reactivity for the porous model is two orders of magnitude greater than for the non-porous model (see Figure 1). This causes O_2 to be consumed less than in the porous case, leading to higher O_2 concentrations in the vicinity of the non-porous surface. The higher concentration of O_2 , combined with high temperatures, leads to an increased concentration of the radical pool, i.e. OH and O, thereby increasing their contribution to CO production.

For the temperatures of 1800–2600 K considered with moist air ($X_{H_2O} = 0.02$), the $C_s + H_2O \rightarrow CO + H_2$ surface reaction makes up most of the remaining CO production at the surface, i.e. in addition to the $C_s + O_2$, $4C_s + OH$, and $C_s + O$ surface reactions. The homogeneous oxidation of highly reactive H_2 produced at the surface, in addition

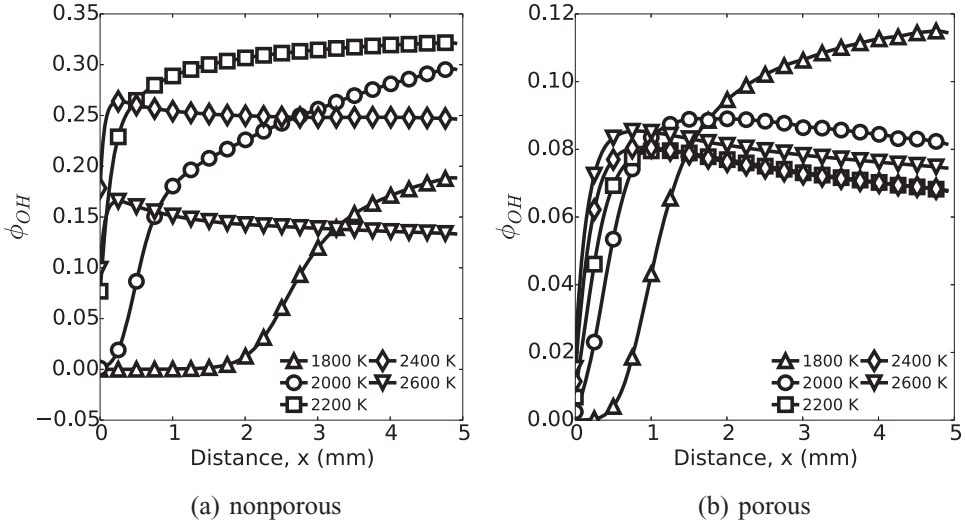


Figure 14. Fraction of CO production due to reaction with OH, for a velocity of 40 m/s and a range of surface temperatures.

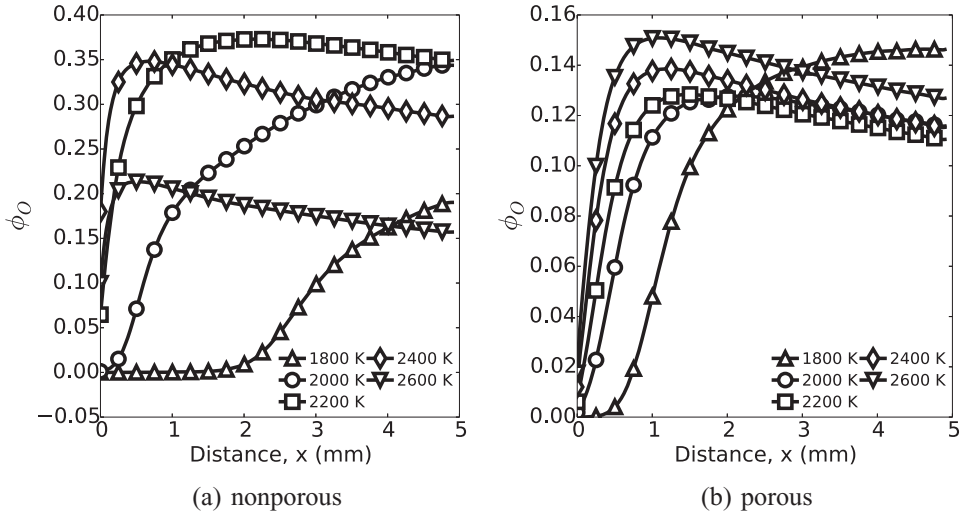


Figure 15. Fraction of CO production due to reaction with O atoms, for a velocity of 40 m/s and a range of surface temperatures.

to the moist CO oxidation pathways, accelerates the production of radicals OH and O. Figures 16(a) and 16(b) show the production of CO due to water for the non-porous and porous cases, respectively. The contribution of the $C_s + H_2O$ reaction increases with increasing temperature for both cases. Water's contribution to net CO production reaches above 60% in the non-porous case. A sudden increase in the non-porous case from 2400 to 2600 K is due to water exceeding the reactivity of OH and O atoms. This is supported by the sudden reduction in OH and O contributions (see Figures 14(a) and 15(a)) in the non-porous case. Water plays less of a role in the porous case due to the dominant role of the $C_s + O_2$ reaction.

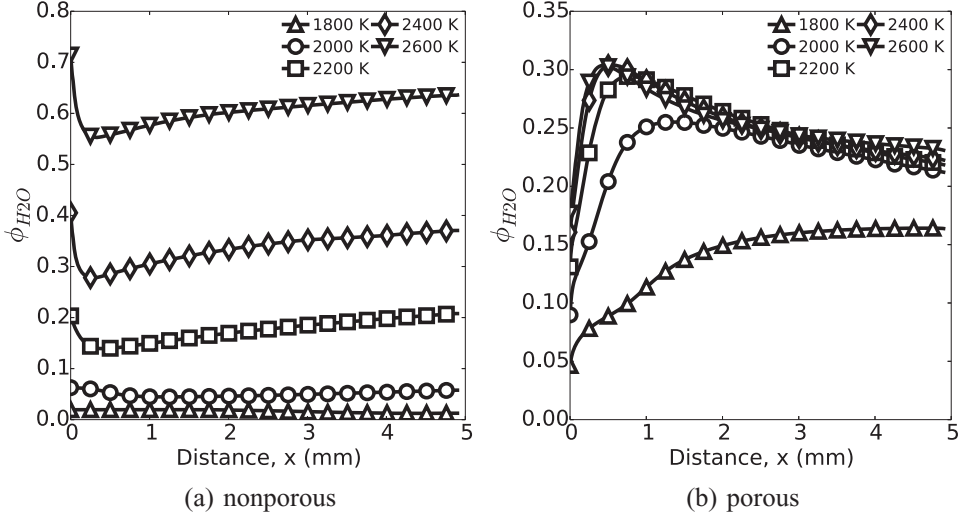


Figure 16. Coupling of gaseous O_2 and CO production: (a) non-porous; (b) porous.

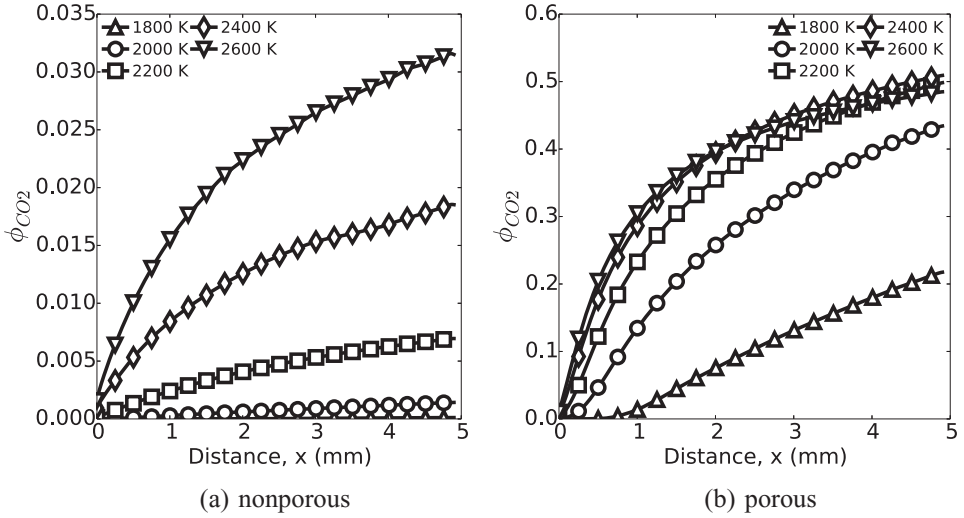


Figure 17. Fraction of CO production due to reaction with CO_2 , for a velocity of 40 m/s and a range of surface temperatures.

Figures 17(a) and 17(b) show the production of CO due to CO_2 , for both the non-porous and porous models, respectively. CO_2 contributes two orders of magnitude less in the production of CO in the non-porous case when compared with the porous case. In the porous case, CO_2 contributes 10 to 50% of CO production whereas in the non-porous case it contributes less than 3%, due mainly to the highly detached CO oxidation reaction front of the porous case. To test if the non-porous $\text{C}_s + \text{CO}_2$ reaction was negligible, the five temperature cases were simulated with the corresponding $\text{C}_s + \text{CO}_2$ surface reactions removed. Figure 18 shows the mole concentration for CO along the surface for cases where the CO_2 reaction was included (shown with a solid line, —) and where the reaction

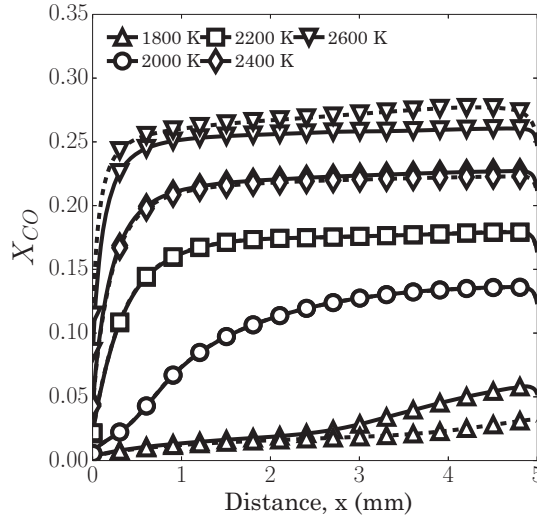


Figure 18. CO concentration along the surface for the $C_s + CO_2$ reaction on (ifig1) and the $C_s + CO_2$ reaction off (—) for the non-porous model with a flow velocity of 40 m/s.

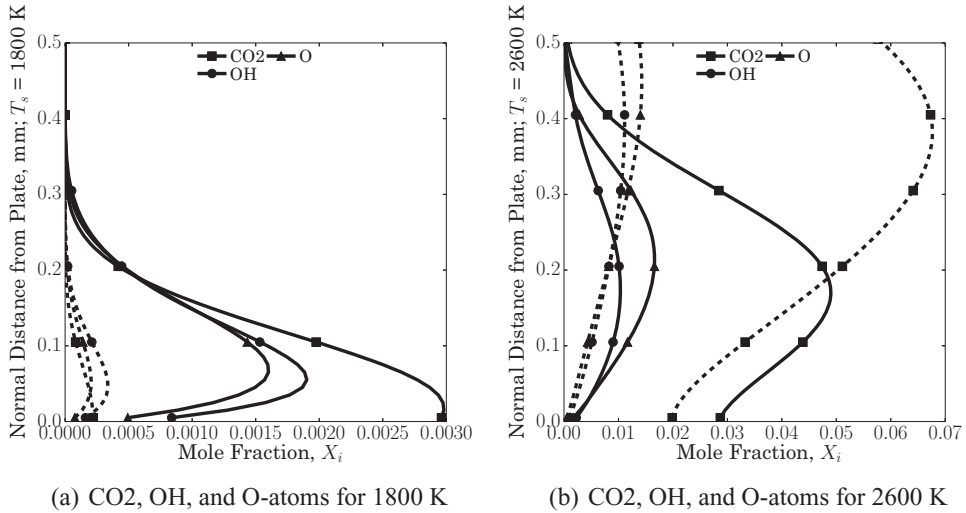


Figure 19. Structure of reacting layer normal to the surface at $x = 4$ mm, for cases with (—) and without (---) the $C_s + CO_2$ surface reaction using the non-porous model.

was removed (shown with a dashed line, ---). As seen from these figures, the CO mole fractions along the surface in the 1800 and 2600 K cases differ due to the exclusion of the $C_s + CO_2$ reaction. However, for temperatures in between these two limits considered, the results show close agreement in both shape and magnitude. To understand the underlying cause for the observed trends better, Figures 19(a) and 19(b) show concentrations of CO_2 , OH, and O atoms in the normal direction to the reacting surface at $x = 4$ mm, for 1800 and 2600 K, respectively, with the CO_2 reaction included (solid line) and excluded (dashed line). When the $C_s + CO_2$ reaction is excluded from the model, the predicted structure of radical species is found to be quite different in both magnitude and shape. This difference

also determines the concentrations of OH and O atoms, which are important reactants for CO production in the non-porous model (see [Figures 14\(a\)](#) and [15\(a\)](#)). Despite the small contribution of $C_s + CO_2$, the present results indicate that the surface reaction that consumes CO_2 is still important and must be retained because of its effect on the radical species O and OH. Therefore, any removal of semi-global surface reactions from the oxidation of carbon surfaces must carefully analyse the complex coupling between homogeneous and heterogeneous reaction pathways.

5. Conclusions

Previously developed carbon surface reaction models were successfully implemented into a finite volume method reacting flow solver (OpenFOAM®) to explore the multidimensional coupling between homogeneous and heterogeneous kinetics. Specifically, in order to explore finite-rate kinetics and flow residence time effects, a reacting carbon surface temperature and free-stream velocity in the ranges 1800 to 2600 K and 30 to 50 m/s, respectively, were analysed. The simulated domain was restricted to 10 mm in length and 1 mm in height with a 5 mm long reacting carbon surface in order to resolve the transport and chemical reaction processes fully.

The results showed interesting coupling between heterogeneous and homogeneous reactions, especially the gas-phase flame attachment and detachment conditions, which are dependent on free stream velocity, surface temperature, and heterogeneous model (or porosity). It was shown that the fractional contributions of semi-global reactions to overall carbon removal and CO production can change drastically depending on the physical conditions. For example, at high porosity, the $C_s + O_2$ reaction dominates at the leading edge of the boundary layer, while the $C_s + CO_2$ reaction was shown to dominate over the trailing edge of the boundary layer. On the other hand, for the low carbon removal rate associated with the non-porous carbon surface reaction model, O_2 , H_2O , and the radical species OH and O were shown to have a dominant effect on the overall carbon removal rate, while the $C_s + CO_2$ reaction made a minimal direct contribution.

Additionally, the importance of the CO_2 reaction for non-porous carbon was tested by either including or excluding this reaction. It was shown that even though $C_s + CO_2$ make a small contribution to the non-porous carbon oxidation rate, inclusion of this reaction has a noticeable effect on the radical pool, and hence can influence the overall carbon removal rate, especially at the low and at the high temperature limits considered. Therefore, any neglect of heterogeneous reactions must be accompanied by careful analysis of the highly coupled nature of the homogeneous and heterogeneous reactions influencing carbon oxidation. This result specifically applies to nozzle ablation simulations, where O_2 and O-atom reactions are often neglected because of their perceived negligible contribution due to low concentrations.

Disclosure statement

No potential conflict of interest was reported by the authors.

Funding

The authors would like to acknowledge the Air-Force High-Energy Laser Joint Technology Office (HEL-JTO) for funding, under the HEL JTO MRI Program [AFOSR-BAA-2010-2]; Ryan Johnson

was supported by the Department of Defense (DoD) through the National Defense Science & Engineering Graduate Fellowship (NDSEG) Program and the Virginia Space Grant Consortium (VSGC) Graduate Fellowship Program.

References

- [1] N. Laurendeau, *Heterogeneous kinetics of coal char gasification and combustion*, Prog. Energy Combust. Sci. 4 (1978), pp. 221–270.
- [2] R.H. Essenhigh, *Fundamentals of coal combustion*, in *Chemistry of Coal Utilization, Second Supplementary Volume*, M. Elliot, ed., Wiley, New York, 1981, pp. 1153–1312.
- [3] C.S. McEnally, L.D. Pfefferle, B. Atakan, and K. Kohse-Hoinghaus, *Studies of aromatic hydrocarbon formation mechanisms in flames: Progress towards closing the fuel gap*, Prog. Energy Combust. Sci. 32 (2006), pp. 247–294.
- [4] H. Wang, *Formation of nascent soot and other condensed-phase materials in flames*, Proc. Combust. Inst. 33 (2011), pp. 41–67.
- [5] A.E. Karatas and O.L. Gulder, *Soot formation in high pressure laminar diffusion flames*, Prog. Energy Combust. Sci. 38 (2012), pp. 818–845.
- [6] D.E. Edwards, D.Y. Zubarev, J. William A. Lester, and M. Frenklach, *Pathways to soot oxidation: Reaction of OH with phenanthrene radicals*, J. Phys. Chem. A 118 (2014), pp. 8606–8613.
- [7] J.A. Keenan and G.V. Candler, *Simulation of graphite sublimation and oxidation under re-entry conditions*, in *AIAA Aerospace Sciences Meeting, 6th Joint Thermophysics and Heat Transfer Conference*, Colorado Springs, CO, 1994. Paper No. AIAA 1994-2083. Available at <http://dx.doi.org/10.2514/6.1994-2083>.
- [8] G.V. Candler, *Nonequilibrium processes in hypervelocity flows: An analysis of carbon ablation models*, in *50th AIAA Aerospace Sciences Meeting including the New Horizons Forum and Aerospace Exposition*, 9–12 January 2012, Nashville, TN. Paper No. AIAA 2012-0724. Available at <http://dx.doi.org/10.2514/6.2012-724>.
- [9] F.E. Fendell, *Burning of spheres gasified by chemical attack*, Combust. Sci. Technol. 1 (1969), pp. 13–24.
- [10] H. Caram and N. Amundson, *Discussion and reaction in a stagnant boundary layer about a carbon particle*, Ind. Eng. Chem. Fund. 16 (1977), pp. 171–181.
- [11] P. Libby and T. Blake, *Theoretical study of burning carbon particles*, Combust. Flame 36 (1979), pp. 139–169.
- [12] M. Matalon, *Complete burning and extinction of a carbon particle in an oxidizing atmosphere*, Combust. Sci. Technol. 24 (1980), pp. 115–127.
- [13] E.T. Turkdogan, V. Koump, J.V. Vinters, and T.F. Perzak, *Rate of oxidation of graphite in carbon dioxide*, Carbon 6 (1968), pp. 467–484.
- [14] D. Rosner, *High-temperature gas–solid reactions*, Ann. Rev. Mat. Sci. 2 (1972), pp. 573–606.
- [15] D. Bradley and G. Dixon-Lewis, *The oxidation of graphite powder in flame reaction zones*, Symp. (Int.) Combust. 20 (1985), pp. 931–940.
- [16] A. Makino, I. Kato, M. Senba, H. Fujizaki, and N. Araki, *Flame structure and combustion rate of burning graphite in the stagnation flow*, Proc. Combust. Inst. 26 (1996), pp. 3067–3074.
- [17] H.K. Chelliah, A. Makino, C.K. Law, I. Kato, and N. Araki, *Modeling of graphite oxidation in a stagnation-point flow field using detailed homogeneous and semiglobal heterogeneous mechanisms with comparisons to experiments*, Combust. Flame 104 (1996), pp. 469–480.
- [18] R.E. Mitchell, R.J. Kee, P. Glarborg, and M.E. Coltrin, *The effect of CO conversion in the boundary layers surrounding pulverized-coal char particles*, Symp. (Int.) Combust. 23 (1991), pp. 1169–1176.
- [19] H.K. Chelliah, *Numerical modelling of graphite combustion using elementary, reduced and semi-global heterogeneous reaction mechanisms*, in *Modeling in Combustion Science*, J. Buckmaster and T. Takeno, eds., Lecture Notes in Physics, Springer-Verlag, Berlin, 1995, pp. 130–147.
- [20] R.I. Acosta, K.C. Gross, and G.P. Perram, *Mid-infrared imaging Fourier transform spectrometry for high power fiber laser irradiated fiberglass composites*, Proc. SPIE 8239 (2012).
- [21] S.Y. Cho, R.A. Yetter, and F.L. Dryer, *J. Comput. Phys.* 102 (1992), pp. 160–179.
- [22] D. Reinelt, A. Laurs, and G. Adomeit, *Ignition and combustion of a packed bed in a stagnation point flow. Part II: Heterogeneous and homogeneous reactions*, Combust. Flame 113 (1998), pp. 373–379.

- [23] J.L. Kassebaum and H.K. Chelliah, *Oxidation of isolated porous carbon particles: Comprehensive numerical model*, Combust. Theory Model. 13 (2009), pp. 143–166.
- [24] P. Thakre and V. Yang, *Chemical erosion of carbon–carbon/graphite nozzles in solid-propellant rocket motors*, J. Propul. & Power 24 (2008), pp. 822–833.
- [25] P. Thakre and V. Yang, *Mitigation of graphite nozzle erosion by boundary-layer control in solid propellant rocket motors*, J. Propul. & Power 25 (2009), pp. 1079–1085.
- [26] D. Bianchi, F. Nasuti, and E. Martelli, *Coupled analysis of flow and surface ablation in carbon–carbon rocket nozzles*, J. Spacecraft Rockets 46 (2009), pp. 492–500.
- [27] D. Bianchi, F. Nasuti, M. Onofri, and E. Martelli, *Thermochemical erosion analysis for graphite/carbon–carbon rocket nozzles*, J. Propul. Power 27 (2011), pp. 197–205. Available at <http://dx.doi.org/10.2514/1.47754>.
- [28] H. Weng and A. Martin, *Multidimensional modeling of pyrolysis gas transport inside charring ablative materials*, J. Thermophys. Heat Trans. 28 (2014), pp. 583–597.
- [29] H. Jasak, A. Jemcov, and Z. Tukovic, *Openfoam: A C++ library for complex physics simulations*, in *International Workshop on Coupled Methods in Numerical Dynamics*, IUC, 2007.
- [30] R.F. Johnson, A.C. VanDine, G. Esposito, and H.K. Chelliah, *On the axisymmetric counterflow flame simulations: Is there an optimal nozzle diameter and separation distance to apply quasi one-dimensional theory?* Combust. Sci. Technol. 187 (2015), pp. 37–59.
- [31] H. Wang, E. Dames, B. Sirjean, D. Sheen, R. Tangko, A. Violi, J. Lai, F. Egolopoulos, D. Davidson, R. Hanson, C. Bowman, C. Law, W. Tsang, N. Cernansky, D. Miller, and R. Lindstedt, *A high-temperature chemical kinetic model of n-alkane (up to n-dodecane), cyclohexane, and methyl-, ethyl-, n-propyl and n-butyl-cyclohexane oxidation at high temperatures, JetSurf version 2.0, 2010; software available at http://web.stanford.edu/group/haiwanglab/JetSurF/JetSurF2.0/Mech_JetSurF2.0.txt*.
- [32] R.J. Kee, J.A. Miller, and T.H. Jefferson, *Chemkin II: A general purpose, problem-independent, transportable, Fortran chemical kinetics code package (SAND 89)*, 1980.
- [33] R.J. Kee, J.A. Miller, and J. Warnatz, *A Fortran computer code package for the evaluation of gas-phase multicomponent transport properties (SAND 86)*, 1986.
- [34] R.I. Issa, *The computation of compressible and incompressible recirculating flows by a non-iterative implicit scheme*, J. Comput. Phys. 62 (1986), pp. 66–82.
- [35] A.G. Tomboulides, J.C.Y. Lee, and S.A. Orszag, *Numerical simulation of low Mach number reactive flows*, J. Sci. Comput. 12 (1997), pp. 139–167. Available at <http://dx.doi.org/10.1023/A:1025669715376>.
- [36] M. Oevermann, S. Gerber, and F. Behrendt, *Euler–Lagrange/DEM simulation of wood gasification in a bubbling fluidized bed reactor*, Particuology 7 (2009), pp. 307–316.
- [37] A. Cuoci, A. Frassoldati, T. Faravelli, and E. Ranzi, *A computational tool for the detailed kinetic modeling of laminar flames: Application to C₂H₄/CH₄ coflow flames*, Combust. Flame 160 (2013), pp. 870–886.
- [38] F.A. Williams, *Combustion Theory*, 2nd ed., Westview Press, New York, NY (1994).
- [39] R. Puri, R.J. Santoro, and K.C. Smyth, *The oxidation of soot and carbon monoxide in hydrocarbon diffusion flames*, Combust. Flame 97 (1994), pp. 125–144.
- [40] H. Guo, P.M. Anderson, and P.B. Sunderland, *Optimized rate expressions for soot oxidation by OH and O₂*, Fuel (2016), pp. 248–252.
- [41] J. Nagle and F. Strickland-Constable, *Oxidation of carbon between 1000–2000°C*, in *Proceedings of the Fifth Conference on Carbon*, Vol. 1, 1962, Pergamon Press, London, UK, pp. 154–164.

Appendix A. Details of the implemented heterogeneous reaction models

A.1. Non-porous reaction model

The specific reaction rate parameters of the non-porous reaction model used in this work are listed in [Table A1](#), which was compiled by Bradley and Dixon-Lewis [15].

Knowing the specific reaction rate parameters listed in [Table A1](#), the mass production rate, w'_i (kg/m²/s), can be calculated by using the modified-Arrhenius expression,

$$k_i = B_i T^{n_i} \exp(-E_i/RT), \quad (\text{A1})$$

with the following surface mass production rate relations:

Table A1. The heterogeneous reaction rate parameters of non-porous carbon as compiled by [15].

Reaction	i	B_i	n_i	E_i
$C_s + OH \rightarrow CO + H$	1	3.61×10^2	-0.5	0
$C_s + O \rightarrow CO$	2	6.65×10^2	-0.5	0
$C_s + H_2O \rightarrow CO + H_2$	3	4.80×10^5	0.0	68,800
$C_s + CO_2 \rightarrow 2CO$	4	9.00×10^3	0.0	68,100
$C_s + \frac{1}{2}O_2 \rightarrow CO$	5	2.40×10^3	0.0	30,000
	6	2.13×10^1	0.0	-4,100
	7	5.35×10^{-1}	0.0	15,200
	8	1.81×10^7	0.0	97,000

$$w'_{OH} = -(p_{OH})k_1, \quad (A2)$$

$$w'_O = -(p_O)k_2, \quad (A3)$$

$$w'_{H_2O} = -(p_{H_2O})^{1/2}k_3, \quad (A4)$$

$$w'_{CO_2} = -(p_{CO_2})^{1/2}k_4, \quad (A5)$$

$$Y = \frac{1}{1 + \frac{k_8}{k_7 p_{O_2}}},$$

$$w'_{O_2} = \left(-\frac{1}{2}\right) \left[\frac{k_5 p_{O_2} Y}{1 + k_6 p_{O_2}} + k_7 p_{O_2} (1 - Y) \right], \quad (A6)$$

$$w'_H = (p_{OH})k_1 \frac{W_H}{W_{OH}}, \quad (A7)$$

$$w'_{H_2} = (p_{H_2O})k_3 \frac{W_{H_2}}{W_{H_2O}}, \quad (A8)$$

$$w'_{CO} = - \left(w'_{OH} \frac{W_{CO}}{W_{OH}} + w'_O \frac{W_{CO}}{W_O} + w'_{H_2O} \frac{W_{CO}}{W_{H_2O}} + w'_{CO_2} \frac{2W_{CO}}{W_{CO_2}} + w'_{O_2} \frac{2W_{CO}}{W_{O_2}} \right). \quad (A9)$$

Here, p_i denotes partial pressure of species i , in atmospheric pressure units.

A.2. Porous model

The reaction rate parameters of the porous model are listed in Table A2.

Table A2. The heterogeneous reaction rate parameters of porous carbon [17].

k	Reaction	B_k	n_k	E_k
1	$C_s + OH \rightarrow CO + H$	1.65	0.5	0
2	$C_s + O \rightarrow CO$	3.41	0.5	0
3	$C_s + H_2O \rightarrow CO + H_2$	2.00×10^8	0.0	64,750
4	$C_s + CO_2 \rightarrow 2CO$	6.00×10^7	0.0	64,300
5	$C_s + \frac{1}{2}O_2 \rightarrow CO$	4.40×10^6	0.0	43,000

Here, the mass production rate, w'_i (kg/m²/s), is calculated using the expression

$$w'_i = \sum_{k=1}^5 \nu_{ik} W_i (\rho Y_k / W_k) B_k T^{n_k} \exp(-E_k / RT), \quad (\text{A10})$$

where subscript i denotes the species of interest, while subscript k denotes the particular reaction step in Table A2. Specifically, W_i is the molecular weight of the i th species of interest, W_k and Y_k are the molecular weight and mass fraction of the reactant species in reaction k , respectively, and ν_{ik} is the stoichiometric coefficient of species i in the k th reaction.

A.3. Temperature dependence of the $\text{C}_s + \text{O}_2$ reaction

It is important to note that the reaction rates of $\text{C}_s + \text{O}_2$, $\text{C}_s + \text{CO}_2$, and $\text{C}_s + \text{H}_2\text{O}$ in both the porous and the non-porous cases increase exponentially with temperature. The one exception to this representation is the non-porous $\text{C}_s + \text{O}_2$ reaction. Figure A1 shows the non-porous reaction rates of carbon with CO_2 and O_2 , normalised to their local maximum within the temperature range of interest. The non-porous model's O_2 reaction rate reaches a maximum near 2100 K, as prescribed by the Nagle and Strickland-Constable [41] model, where the number of available or active sites varies with temperature. No other surface reactions with gaseous species, in either the non-porous or the porous models, exhibit a local maximum within the surface temperatures of interest.

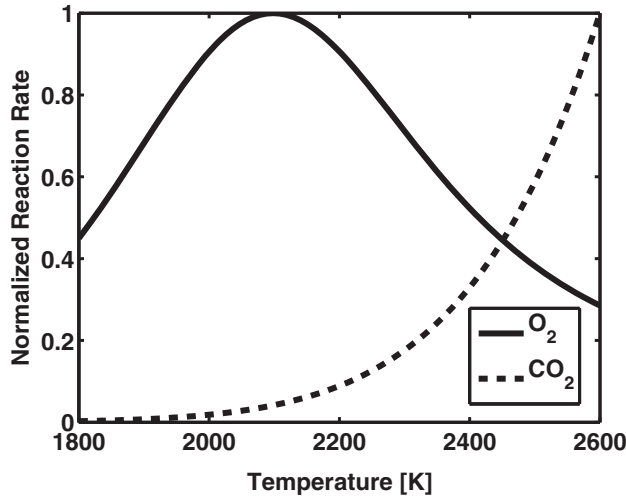


Figure A1. Reaction rates for non-porous O_2 and CO_2 reaction rates (normalised to peak value) showing local extrema for O_2 and a continuous increase for CO_2 .